# Effect of Yaw Angle on Drag Over Clean Rectangular Cavities

*Dhaval Shiyani[1,] Peter Disimile[2]

[1] University of Cincinnati, Cincinnati, OH, USA, shiyandr@mail.uc.edu
[2] University of Cincinnati, Cincinnati, OH, USA, peter.disimile@uc.edu
Corresponding Author: Dhaval Shiyani

## ABSTRACT

The effect of yaw angle on the drag generated by the presence of a clean sharp edged rectangular cavity embedded in a fully developed turbulent boundary layer, generated over a flat plate, was computationally studied using OpenFOAM. Majority of research into cavity flows focus on the unsteady pressures and resulting acoustic signature generated by cavities and potential acoustic suppression techniques. However, the drag caused by these surface cutouts can be substantial, resulting in the generation of shear layer oscillations which could alter the performance of the vehicle containing such surfaces, and potentially produce damaging structural loading and therefore needs to be studied in detail. Numerous experimental studies have been performed that suggest a flow transition within the cavity when a critical yaw angle has been exceeded. To develop an improved understanding of the flow phenomena involved, steady state computations were performed. To this end steady-state simulations using OpenFOAM, an open source computational package, is carried out for cavities with an *L/D* ratio of 16.25 and *L/W* of 8.25, at $\phi$ 90$^0$, for various yaw angles ($\phi$) at an incoming freestream velocity of 25 m/s. In the current study, $\phi$, of 0$^0$, 30$^0$, 45$^0$, 60$^0$, 75$^0$, and 90$^0$ have been studied. The steady pressure contours on the cavity faces are computed and analyzed along with computed drag coefficient and compared to the experimental measurements of Weighardt [1]. Although differences are noted at the lower angles, above 50$^0$ the drag profile is in good agreement. The pressure profiles and drag data suggest a critical change in cavity behavior when the flow transitions from an open type moving towards the closed type.

*Keywords:* Cavity, Drag, Yaw, Computational Fluid Dynamics (CFD), OpenFOAM, k-epsilon, three-dimensional

------------------------------------------------------------------------------------------------------------------------

------------------------------------------------------------------------------------------------------------------------

## NOMENCLATURE:

| | |
|---|---|
| $L$ | Length of cavity (mm) |
| $D$ | Depth of Cavity (mm) |
| $W$ | Width of Cavity (mm) |
| $L_p$ | Incoming plate length, 137.5$L$ (m) |
| $x$ | Longitudinal direction |
| $y$ | Vertical direction |
| $z$ | Transverse direction |
| $p$ | Pressure (Pa) |
| $\rho$ | Density (kg/m$^3$) |
| $P$ | $p/\rho$ (Pa m$^3$/kg) |
| $U_\infty$ | Freestream Velocity (m/s) |
| $U$ | Local Mean Velocity (m/s) |
| $\phi$ | Yaw angle ($^0$, degrees) |
| $C_d$ | Coefficient of Drag |
| $L/D$ | Length to Depth ratio |
| $L/W$ | Length to Width ratio |
| $\delta$ | Boundary layer thickness (mm) |
| $\delta^*$ | Displacement layer thickness (mm) |
| $\theta$ | Momentum layer thickness (mm) |
| $H$ | Shape Factor |

| | |
|---|---|
| $k$ | Turbulent kinetic energy ($m^2/s^2$) |
| $\varepsilon$ | Turbulent dissipation rate ($m^2/s^3$) |
| $\omega$ | Specific rate of dissipation (1/s) |
| $y^+$ | Dimensionless wall distance |
| $u^+$ | Dimensionless velocity |
| $u_\tau$ | Friction velocity (m/s) |

# I.   INTRODUCTION

Drag reduction is one of the major design parameters driving the development of aircrafts. Even a minor decrease in the generated drag can substantially reduce the fuel consumption, thus yielding a better carbon footprint and slashing transportation costs as well. One source of drag generation in aircrafts is a result of depressions and cutouts in the external surface due to the presence of cavities, rivets, landing gear bays, weapons bays, etc. By some estimates, these can contribute up to 3% of total drag generated in a commercial aircraft [4].

Cavity flows have long been a problem carefully studied [2][3][4][7][9] because of their importance in aircraft design, weapons bay designs, automotive designs, and many more areas of interest. However, a major percentage of these studies have focused on the noise generated by such flow fields and techniques to achieve efficient suppression of these noises. In addition, most studies have only considered rectangular cavities oriented at yaw angles of either $0^0$ or $90^0$. When the yaw angle was set to $0^0$ the cavity was observed to be quasi-two dimensional (i.e., the major axis of the cavity is perpendicular to the oncoming flow), whereas the $90^0$ orientation is highly three-dimensional (3D). [10][11] Since the flow field within the cavity was substantially different the contribution of surface cutouts at yaw to drag generation can be considerable. The main studies that have dealt with this issue have been limited to either overall drag increments contributed by single or multiple holes, two-dimensional (2D) studies on pressure oscillations or experimental results using force balance data. Only a handful of studies have been carried out on the effect of yaw angles on drag generation and even fewer of these were computational studies [4][7][12].  This study will focus on the contribution to drag due to rectangular cavities and the effects of yawed cavity geometries on drag levels. The current investigation is being conducted using 3D computational fluid dynamics (CFD) applied to a sharp edged rectangular cavity immersed in a fully developed turbulent boundary layer. The following section provides a brief overview on the various types of cavity flow fields.

## 1.1. Background

Cavity flows are classified into three basic types; open cavity flows, closed cavity flows, and transitional cavity flows. As presented in figure 1, open cavity flows occur when the shear layer separating off the sharp leading edge impinges directly on to the trailing edge without impinging on the cavity floor. Whereas cavity flows are determined to be closed when the shear layer separates off the leading-edge, impinges and attaches on the cavity floor, and then separates off the floor as it continues towards the trailing edge. A transitional cavity flow field occurs when the flow moves from an open type to a closed type.
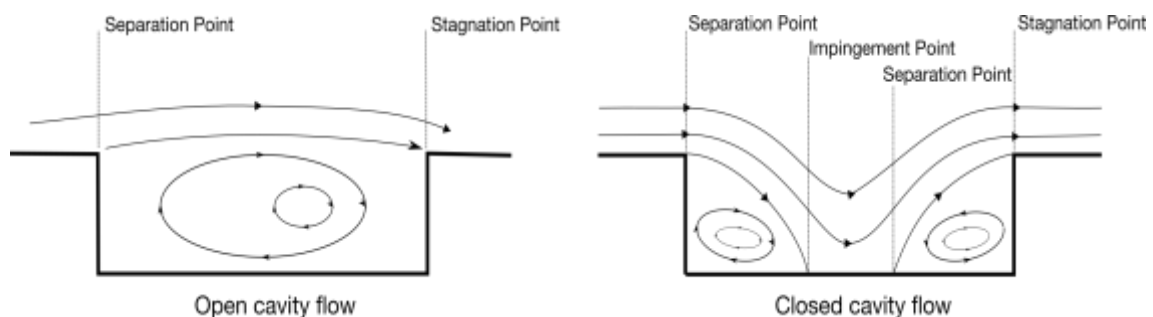


**Figure 1.** Classification of Cavity flows [4][5]

Classification of cavity flow is also dependent on the Length/Depth (*L/D*) and the Length/Width (*L/W*) ratios of the cavities. As the *L/D* ratios are increased, the flow transitions from open to closed type. This intermediate state of the flow is referred to as transitional cavity flow. The typical ranges of *L/D* ratios for all three types of cavity flows mentioned above are listed below in table 1.

**Table 1.** Cavity Flow types [4][5]

| *L/D* Ratio | $\leq$ (7-9) | 8-11 | $\geq$ (10-14) |
|---|---|---|---|
| Classification | Open | Transitional | Closed |

In addition to these descriptions, cavity flows can also be termed as shallow or deep type. Shallow flows occur when the length is greater than the depth ($L/D > 1$) and deep flows occur when the depth is greater than the length ($L/D < 1$). Shallow cavity flows have been studied in this investigation. The incoming free stream velocity is kept at 25 m/s and the cavity dimensions, *L*, *W* and *D* have been kept constant in the current study and only orientation of the cavity, $\phi$, i.e., the yaw angle is varied from $0^0$ - $90^0$. Due to this yaw variation, the flow goes through all 3 types of flow classification, i.e. open, transitional and closed. The effective *L/W* ratios determine the three-dimensionality of the cavity. As the flow transitions from a low *L/W* ratio to a higher value the cavity flow type also transitions from open towards the closed type. The dimensions of the geometry and computational domain used in the current simulations is shown in figure 2. The cavity orientation presented in figure 2 is for $\phi$ of $0^0$, that is when the major axis of the cavity is perpendicular to the incoming flow vector. As the geometry is rotated clockwise to where the major axis of the cavity is tangential to the incoming flow vector the cavity is now at a $90^0$ yaw angle. As the cavity rotates from these baseline orientations, three dimensional effects on the flow becomes evident.

## II. NUMERICAL METHOD

A steady-state solver, provided in the OpenFOAM [16] library, called simpleFoam, was used to simulate the incompressible, turbulent flow conditions used in this study. The simpleFoam solver uses the SIMPLE (Semi-Implicit Method for Pressure-Linked equations) algorithm to solve the Navier-Stokes (NS) equations. It solves the NS equations for mass and momentum (equations (1) & (2), respectively). Since the flow in the current study is assumed to be isothermal, temperature is not taken into consideration, and therefore the energy equation is not solved.

$$\nabla \cdot \left( \rho \vec{U} \right) = 0 \tag{1}$$

$$\nabla \cdot (\vec{v}\vec{v}) - \nabla \cdot (v \nabla \vec{v}) = -\nabla p \tag{2}$$

Second order, Gaussian integration is used to calculate the divergence and the gradient terms in these equations. The pressure term is solved using the generalized geometric-algebraic multi-grid solver (GAMG) while the velocity and turbulence parameters, *k* and $\varepsilon$ for this study, are solved with the smooth Solver. Since all the solvers used required smoothing, a GaussSeidel smoother was specified.

## III. COMPUTATIONAL METHOD

The following section will discuss the computational method used for the simulations. The focus is on the meshing strategy, boundary conditions and turbulence properties.

### 3.1 Domain

An inlet flat plate is used to develop turbulent boundary layer leading up to the cavity. To ensure that the inlet plate length was sufficient to develop a fully turbulent boundary layer, the inlet length was chosen based on the experimental work of Weighardt [1]. It is important to make the flow within the cavity independent of the influences of domain boundaries on the top and the side, since these are considered free-stream atmospheric conditions. Hence the vertical height of the domain was maintained at $10D$ and the side-walls of the domain are at $5D$ from the cavity side-walls. The effect of wall boundaries at this distances on the cavity was not observed. The effect of the top wall on the flow field within the cavity is also not prominent at the distance chosen (see section 4). The transverse direction has two side plates along the length of the domain. These plates are at $5D$ from the cavity side-walls on either direction (see figures 2a and 2b). The *L/D* and *L/W* ratios mentioned in this study are the effective *L/D* and *L/W* ratios at a $\phi$ of $90^0$, since the *L/D* and *L/W* ratio changes due to the change in *L* and *W* w.r.t $\phi$.

### 3.2 Boundary Conditions and Convergence

The boundary conditions used for all the simulations are, velocity inlet at inlet; pressure outlet at outlet; walls on the incoming flat plate, cavity faces, and exit flat plate; symmetry on the domain sidewalls and top wall.
Residuals of the velocity components, the turbulence parameters, and pressure were monitored and convergence threshold of 1e-05 was set. Along with the residuals, continuity was also monitored throughout the simulation and the simulation was deemed converged when the continuity stabilized to a constant value and the residuals dropped below the threshold of 1e-05.

### 3.3 Incoming Boundary Layer

The upstream boundary layer parameters were calculated 1mm upstream of the cavity leading edge. The boundary layer parameters of the incoming flow help determine if the flow is turbulent and fully developed.

Figure 3a shows the incoming boundary layer profile for an inlet flat plate length of 4.4m which is correlated to 137.5*L*, and yields a boundary layer thickness $\delta$ of 71.46 mm. The incoming boundary layer matches well with 1/7th power law and with Weighardt's [1] incoming boundary layer implying that the incoming boundary layer in terms of its size is similar to that of Weighardt's [1].
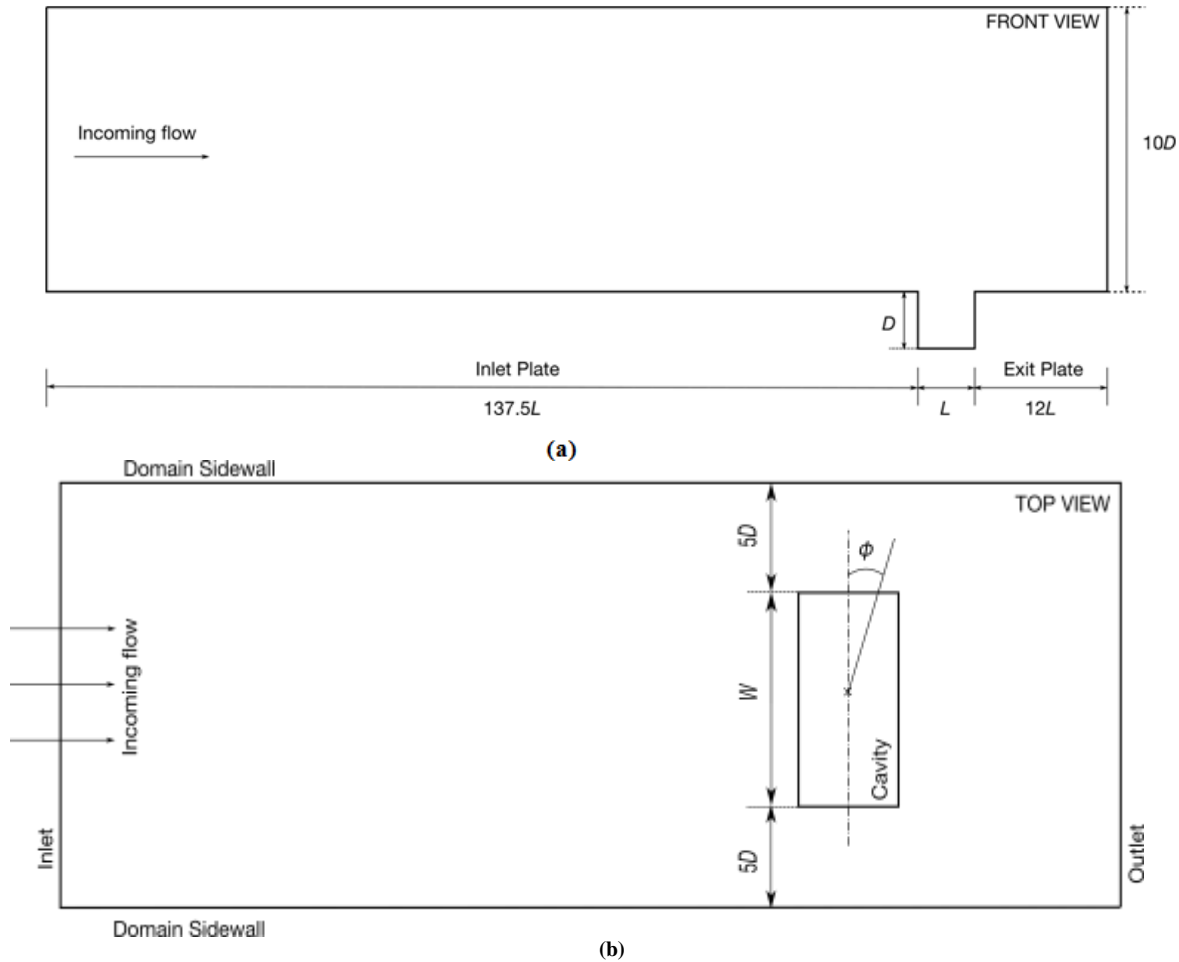


**Figure 2.** Cavity & Domain dimensions at $\phi\,0^0$ (a) Front View (b) Top View (Not to scale)

Figure 3b shows the law of the wall profile for the incoming boundary layer over the 4.4m long flat plate 1mm before the cavity leading edge. Since the $k$-$\varepsilon$ turbulence model was used for the study, a $y^+$ of 30 was chosen for the first mesh node away from the wall faces. This $y^+$ value is recommended for $k$-$\varepsilon$ turbulence models, since the turbulence model utilizes wall-functions to compute the parameters in the viscous sub-layer. This resulted in the viscous sub-layer not being solved numerically. The plot shows the incoming boundary layer follows the law of the wall in the log-law region.

Applying equation 6, the numerical integration of the velocity profile, was used to calculate the boundary layer parameters, $\delta^* \square$ and $\theta$, which are defined by equations 3 and 4 for incompressible flows [8]. The shape factor, *H*, was then computed using equation 5 [8].

$$\delta^* = \int_0^\delta \left(1 - \frac{U(y)}{U_\infty}\right) \mathrm{d}y \tag{3}$$

$$\theta = \int_0^\delta \frac{U(y)}{U_\infty}\left(1 - \frac{U(y)}{U_\infty}\right) \mathrm{d}y \tag{4}$$
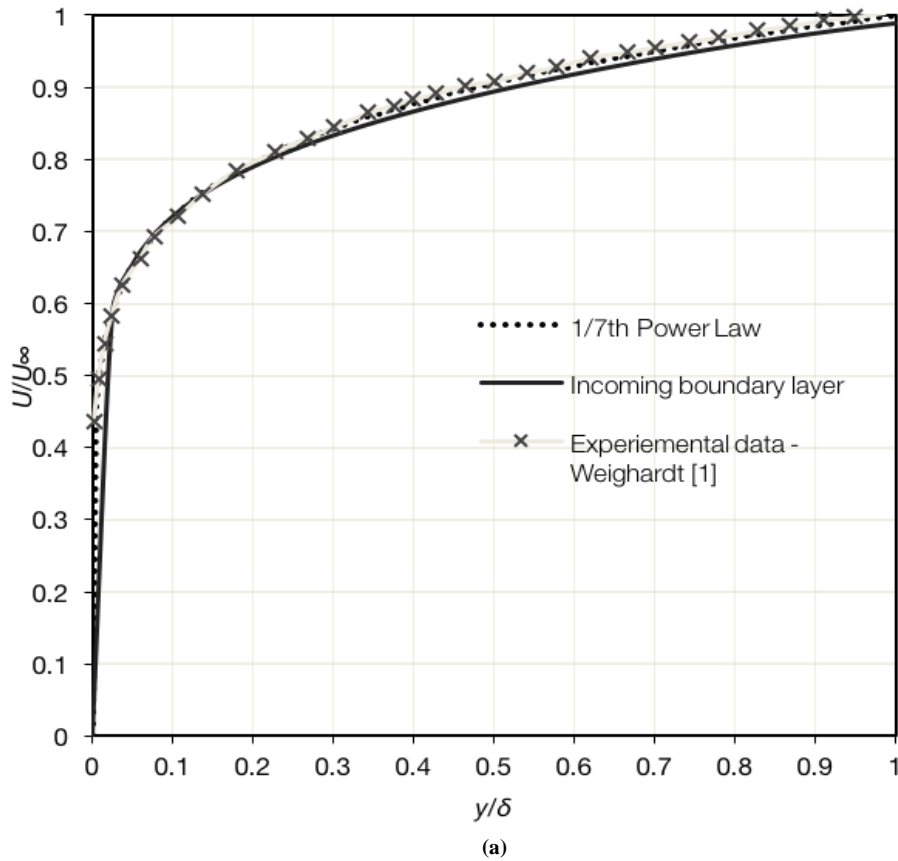
$$H = \frac{\delta^*}{\theta} \tag{5}$$

$$\int_a^b \mathrm{f}(x)\mathrm{d}y \sim \frac{1}{2}\sum_{i=1}^N (x_{i+1} - x_i)\left(\mathrm{f}(x_{i+1}) + \mathrm{f}(x_i)\right) \tag{6}$$

In equation 6, *a* and *b* is the interval, which for the current case spans the length of the boundary layer, hence *a* is *0* and *b* is *δ*. This is further divided into several smaller intervals using *i*. From the equations above, i.e. 3, 4, 5, and 6, the values were obtained for the incoming boundary layer profile over an inlet plate length of 4.4m are listed in table 2.

The shape factor, *H*, along with the other boundary layer parameters in table 2, the velocity profile in figure 3a and the log-law profile in figure 3b support the notion that the incoming boundary layer is fully developed and turbulent.

**Table 2.** Boundary layer parameters

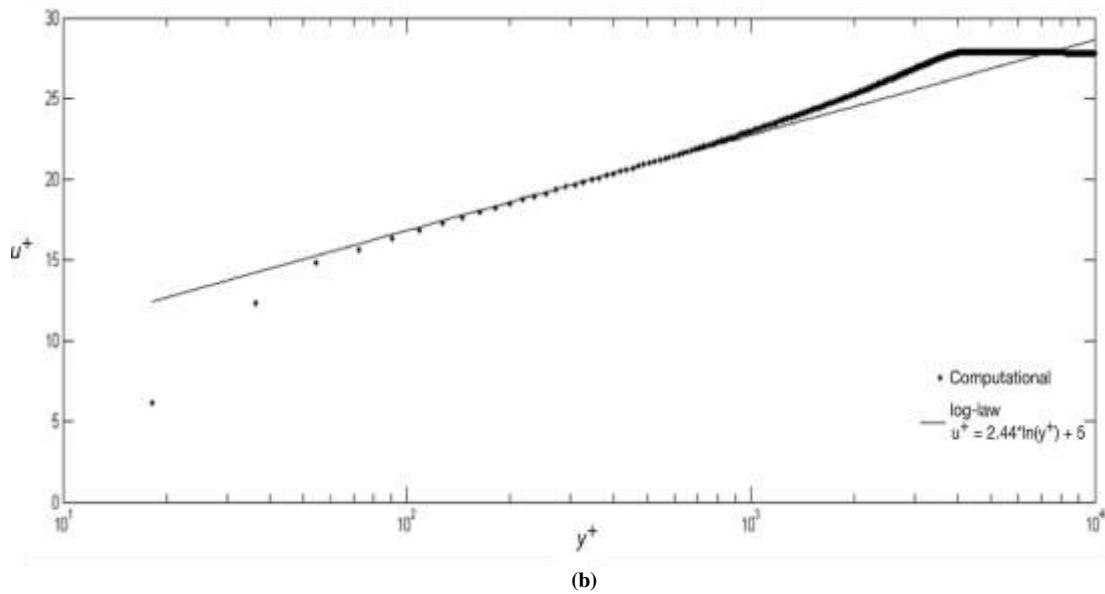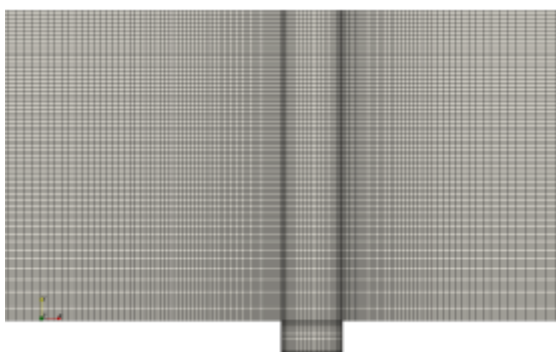| Boundary layer parameter | Value |
|---|---|
| $\delta$ | 71.46 mm |
| $\delta^*$ | 17.36 mm |
| $\theta$ | 11.58 mm |
| $H$ | 1.49 |
| $\Delta u^+$ | 2.3 |
| $Re_{Lp}$ | 8,593,750 |
| $Re_\theta$ | 22,617 |



(a)

**(b)**

**Figure 3** (a). Incoming boundary layer (b). Log law comparison of the incoming boundary layer, where k = 0.41 & C$^+$ = 5
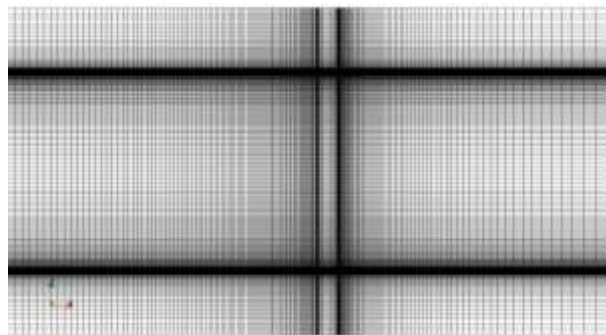
### 3.4 Mesh

A non-uniform, structured mesh was generated for all the yaw angles, with an approximate 5 million cells in the domain. The 3D Cartesian grids are generated with node clustering at the walls and in the shear layer region. The finer grid in these regions capture the high velocity and pressure gradients due to the shear layer oscillations and the influence of the boundary layer. Some basic mesh statistics are presented in table 3, including the aspect ratio of the mesh, which is ratio of the length of the longest edge to the shortest edge. The total number of cells within the cavity is kept the same for all yaw angles. A $y^+$ of 30 was maintained for all the wall regions. Since $k$-$\varepsilon$ turbulence model was used, the near wall region is modelled using wall functions which makes the discretization of near wall regions with the mesh redundant thus yielding a higher $y^+$ value. Details on the $k$-$\varepsilon$ model selected are presented under the turbulence model section below. At least 10 nodes were placed within the incoming boundary layer based on previous simulation experience.

The mesh images presented in figures 4a – 4e, show how the mesh has been generated and the clustering applied. Due to a very large domain, the finer grading used within the cavity needs to be viewed separately, as shown in figures 4c and 4e. The domain has been meshed to have finer clustering towards the cavity in the *x* and *z* directions and towards the walls in the *y* direction, as shown in figures 4a, 4b, and 4d. Figure 4d also shows the mesh for a yawed cavity. The cavity has been rotated within the domain but the mesh nodes on the domain are kept the same as for a non-yawed cavity, yielding to some skewness in the mesh, but with the advantage of mesh cells in the direction of the flow.
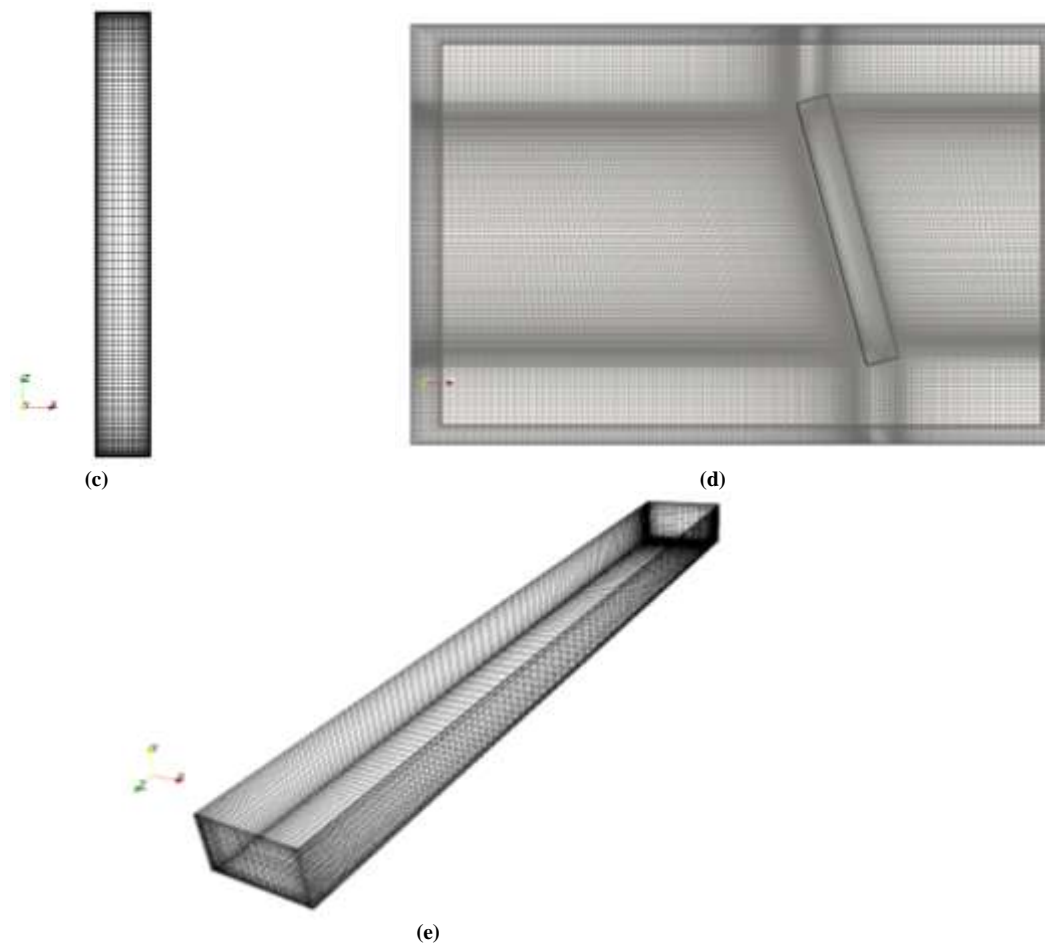


**(a)**



**(b)**

**(c)**

**(d)**

**(e)**

**Figure 4.** (a). Mesh view, *z* axis coming out of the plane, at $\phi 0^0$ (b). Mesh view, *y* axis coming out of the plane, at $\phi 0^0$ (c). Mesh on cavity floor, *y* axis coming out of the plane, at $\phi 0^0$ (d). Mesh view, *y* axis into the plane, at $\phi 30^0$ (e). Mesh on the cavity faces, at $\phi 0^0$

**Table 3.** Mesh parameters

| $\phi$ | Cells | Cells within the cavity | Max. Aspect Ratio |
|---|---|---|---|
| 0 | 4,764,000 | 84000 | 86.1062 |
| 30 | 4,764,000 | 84000 | 102.365 |
| 45 | 4,764,000 | 84000 | 126.861 |
| 60 | 4,764,000 | 84000 | 181.025 |
| 75 | 4,764,000 | 84000 | 351.678 |
| 90 | 4,764,000 | 84000 | 115.741 |

### 3.5 Turbulence Model

The $k$-$\varepsilon$ is a two-equation model which includes two extra transport equations to measure convection and diffusion effects of turbulent energy. The turbulence kinetic energy, $k$ and the turbulent dissipation, $\varepsilon$, are the variables that are transported in this model. The investigation will use the 'Standard' $k$-$\varepsilon$ model formulated by Launder and Sharma [13]. Two other models were also tested during this investigation, namely $k$-$\omega$ and $k$-$\omega$ SST.

The $k$-$\omega$ [14] is built as an improvement to the standard $k$-$\varepsilon$ model whereas the $k$-$\omega$ SST [15] is an improvement on the standard $k$-$\omega$ model. $k$-$\omega$ SST uses $k$-$\varepsilon$ to model turbulence in the outer region of the boundary layer, due to its accuracy in predicting the freestream region; while using $k$-$\omega$ to model turbulence in the inner region of the boundary layer. This improves the model's prediction in the outer regions when compared to standard $k$-$\omega$. The results from all three turbulent model comparison was within the margin of error and hence the more universally used, $k$-$\varepsilon$ was chosen for this study.

A uniform freestream inlet turbulence intensity of 5% was chosen for the present study based on published literature and past simulations.

## IV. RESULTS AND DISCUSSION

Examining the results of pressure variation on cavity faces with respect to yaw angles will provide additional insight into the effect of varying yaw angle on the surface pressure generated within the cavity and corresponding drag. The figures presented below are arranged so that a face of the cavity is the focus in one group and where variation with yaw angle is observed and studied. Figures 5-8 show the pressure contours on the front wall, rear wall, floor & all cavity faces respectively. In an incompressible OpenFOAM [16] simulation, the pressure is divided by the density term to yield the pressure for the simulation as,

$$P = \frac{p}{\rho}$$

(7)

where $p$ is the pressure and $\rho$ is the density.

The pressure ($P$) shown in all the figures below is in terms of the computed absolute pressure divided by the density. Also, the pressure field has been locally scaled in each of these figures to show the variation of pressure on each of the faces in greater contrast. However, figure 8 gives us the pressure values scaled to all the faces of the cavity and helps understand the relative differences in pressure on various faces of the cavity. As can be seen from the images below, the effect of pressure on cavity front wall or floor may seem exaggerated due to the contour coloring but it is worth visiting figure 8 to notice that the pressure variation within the cavity is only large on some faces, i.e. rear wall and not as pronounced as it may seem on others, namely front wall & the floor.

Figures 5a, 6a, and 7a have axis superimposed on the contours to get a better judgement of the cavity dimensions. The length, depth & width are normalized with the cavity length, *L*, to provide a relative scale of the cavity with respect to the length of the cavity.

The faces at various yaw angles for the cavity front walls and the cavity rear walls are oriented in such a manner that the full face always remains parallel to the plane of the paper and the viewing axis is titled by the corresponding yaw angle. This helps give a better idea of the pressure distribution without distorting the contour due to perspective scaling. The orientation of the cavity can be understood from figure 8 along with figures 4a, 4b, 4d, 4e, and figure 2. Taking figure 4a as a reference image, the positive *x*-axis is the direction of the flow, positive *y*-axis is the direction upwards starting from the cavity floor & the positive *z*-axis is along the width of the cavity and coming out of the plane of the paper when $\phi = 0^0$.

From the pressure contours on the cavity front walls, in figure 5, we can see the effect of three-dimensionality as the cavity is yawed w.r.t. the flow. The pressure variation is symmetric about the transverse axis, i.e. perpendicular to the oncoming flow, and there is a region of high stagnation, uniformly distributed along the cavity trailing edge. The uniformity in the transverse direction suggest little to no three-dimensional effects on the mean flow. This can be observed on both the front and rear walls of the cavity in figures 5a and 6a.

Though in terms of absolute pressure values, the difference in pressure along the face is very small for non-yawed cavities, i.e., $0^0$ and $90^0$. But as the cavity is yawed w.r.t. the flow the pressure differential on the cavity face increases considerably as can be seen in figures 5c, 5d, and 5e.

Figure 6 shows the pressure distribution on the rear wall of the cavity at various yaw angles. In the rear wall pressure, we can observe a much larger pressure differential across the face. This is to be expected and is due to the flow impinging directly on the wall in both open and closed type of flows. This impingement point moves as the cavity is yawed from $0^0$ to $90^0$. The impingement is much more uniform for non-yawed cavities, $0^0$ & $90^0$, as seen in figure 6a and 6f, except for wall effects due to the side wall. This shows that the cavity is highly 2D at $\phi$ of $0^0$ and $90^0$, however at $90^0$ the wall effects from the side walls are more pronounced due to the larger effective *L/W* ratio at that angle.

From figures 5 and 6, it can also be observed that the maximum pressure on the cavity front wall and rear wall occurs at $\phi\, 75^0$ and $\phi\, 30^0$ respectively. As the yaw angle increases the front wall turns toward the trailing edge of the flow while the rear wall turns away. Due to this geometric shift, the high stagnation region on the trailing side of the cavity impinges more on the front wall as the yaw angle is increased, as can be seen from figures 8b and 8e.
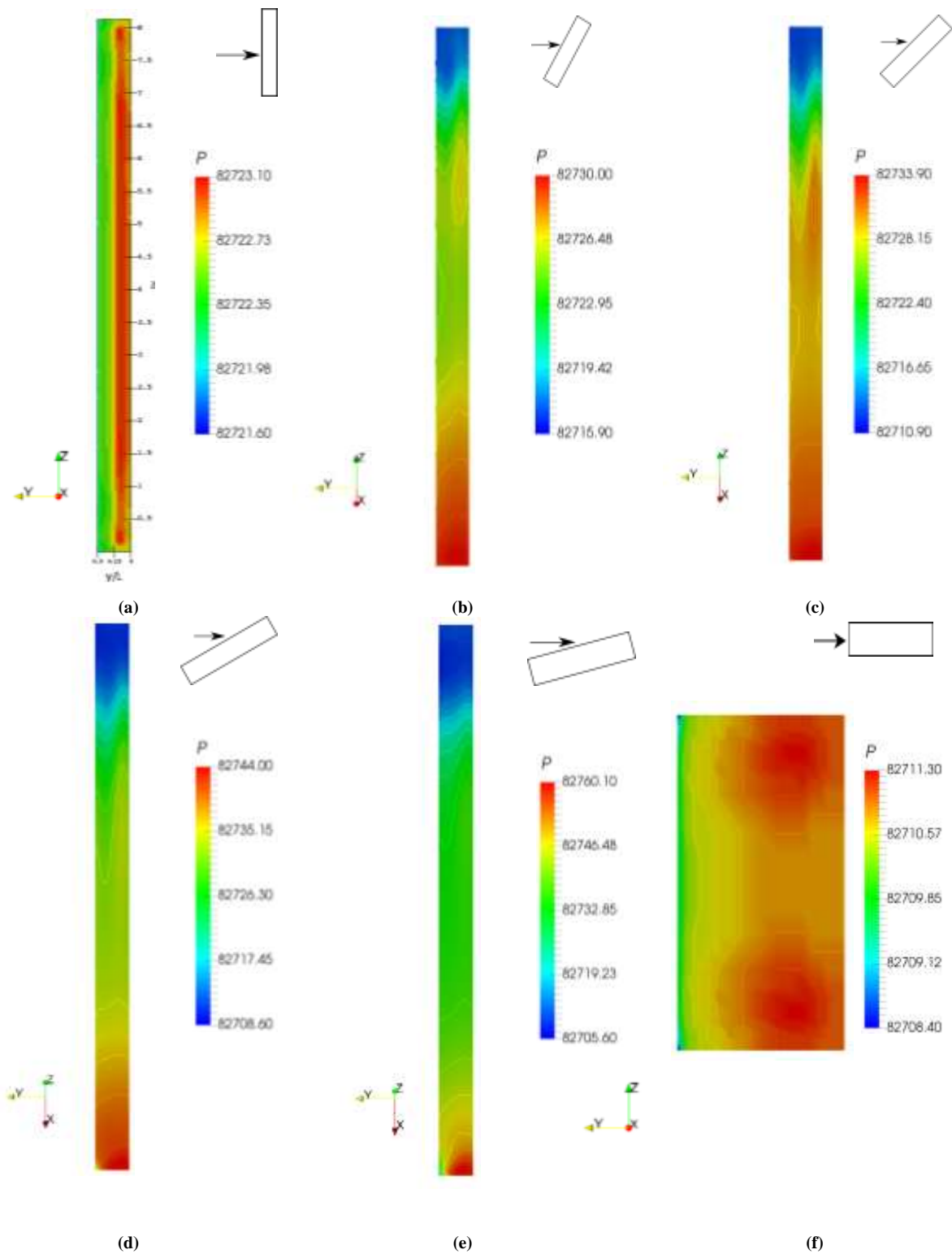
**(a)** **(b)** **(c)**

**(d)** **(e)** **(f)**

**Figure 5.** Pressure contours of cavity front wall at (a) $\phi\, 0^0$ (b) $\phi\, 30^0$ (c) $\phi\, 45^0$ (d) $\phi\, 60^0$ (e) $\phi\, 75^0$ (f) $\phi\, 90^0$
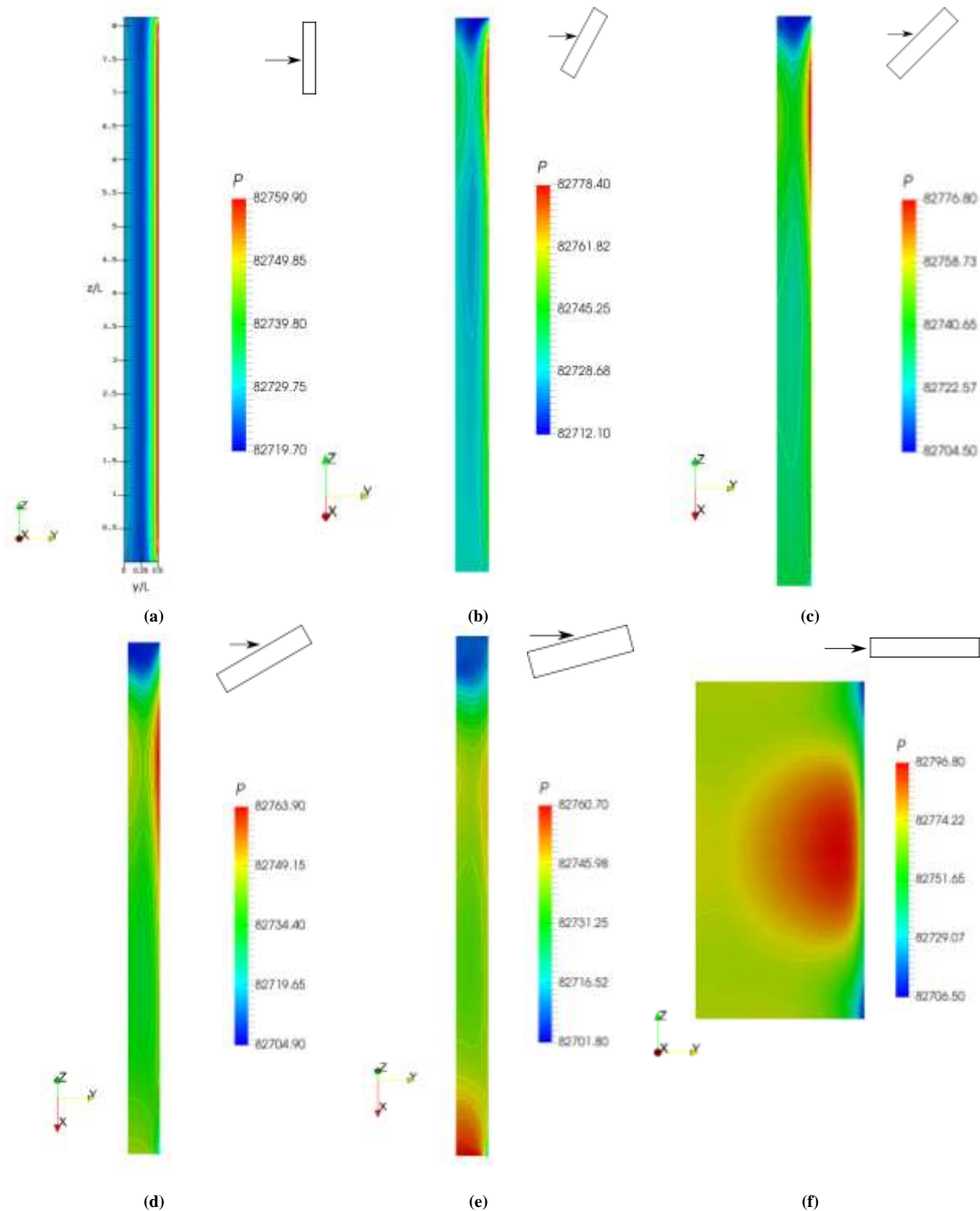
**Figure 6.** Pressure contours of cavity rear wall at (a) $\phi 0^0$ (b) $\phi 30^0$ (c) $\phi 45^0$ (d) $\phi 60^0$ (e) $\phi 75^0$ (f) $\phi 90^0$

Figure 7 shows the distribution of pressure on the cavity floor at various yaw angles. The rotation in figure 7 is about the *y*-axis with the positive *y*-axis going into the plane of the paper when the cavity is rotated counter-clockwise using the left-hand rule. It can be observed once more, in figure 7a, that the pressure differential along the cavity floor is much smaller compared to other yaw angle configurations. The flow impinges on the trailing edge of the cavity floor yielding a high-pressure region along the edge which is symmetric and two-dimensional at $\phi 0^0$. This high-pressure region moves along the trailing edge of the cavity floor as the cavity moves through various yaw angles. The pressure distribution on the cavity edges at yaw angles is higher towards the sides that are turned into the flow (farther along positive *z*-direction) and decreases towards the side that are turned away

from the flow (closer to the origin in the *z*-direction). Figure 7b shows that at a yaw angle of $30^0$ the side of the trailing edge turned towards the incoming flow experiences a greater stagnation and thus higher pressure than the one turned away. This can be attributed to the thickness of the boundary layer in which the edges of the cavity are immersed. As the yaw angle increases the boundary layer thickness along the trailing edge, or any edge for that matter, is different due to the difference in the longitudinal position of the edges. The boundary layer is thicker downstream which leads to lower energy flow towards the downstream side of the walls. This energy differential may create a pressure differential along the edge of the cavity when turned against the oncoming flow. This can be further seen in figures 6b, 6c, 6d, and 6e.
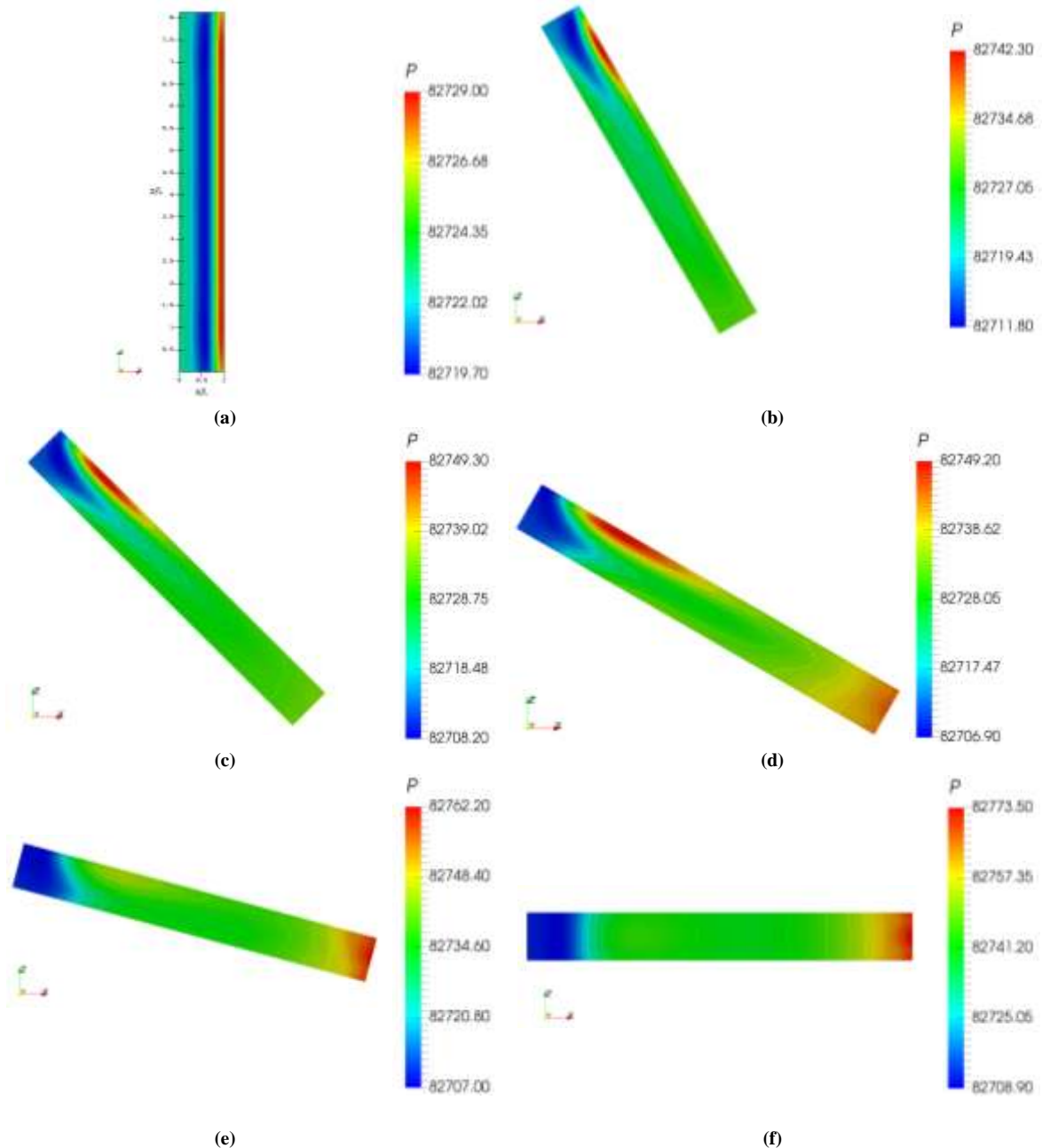


(a)                                                                                (b)

(c)                                                                                (d)

(e)                                                                                (f)

**Figure 7.** Pressure contours of cavity bottom wall at (a) $\phi\, 0^0$ (b) $\phi\, 30^0$ (c) $\phi\, 45^0$ (d) $\phi\, 60^0$ (e) $\phi\, 75^0$ (f) $\phi\, 90^0$

This pressure imbalance along the *z* direction on the trailing edge is only visible when the flow is highly yawed, i.e. in the middle range of yaw angles studied in this work. The magnitude of the pressure differential along the cavity edge in the *z*-direction is also not as high as compared to the magnitude of the high-pressure differential region in the entire cavity, including all faces, as seen in figures 5-8.

From figures 5e, 6e, and 7e, it can also be observed that this shift in stagnation point of the impinging shear layer starts becoming more symmetric at yaw angle of $75^0$. The flow starts to transition from open to closed type

with increasing yaw angle. Also, a completely closed flow was observed for the effective *L/D* and *W/D* ratios studied in this work at $\phi\, 75^0$ and $90^0$. This can be seen from the pressure distribution in the cavity in figures 8e and 8f, where there is a high stagnation region on the rear face of the cavity. This region is due to the second vortex that forms once the shear layer from the cavity floor hits the cavity trailing edge. At a highly-yawed configuration, i.e. $\phi\Box 30^0$-$60^0$, the cavity side-wall and the rear-wall are both facing the oncoming flow either in parts or in entirety. This lends to the asymmetry of the flow and makes an effective trailing edge hard to define. As the flow approaches symmetry at $\phi\, 75^0$ the trailing edge of the cavity starts becoming more defined as it usually is just one edge, as can be seen in figure 7e. As the yaw angle approaches $90^0$, the symmetry in the flow is restored and the three-dimensional effects of side walls appear on the pressure field. The shear layer for the $75^0$ and $90^0$ configurations does reattach on the cavity floor as can be seen from figures 7e, 7f, 8e, and 8f. This reinforces the notion that the flow transitions from an open to a closed regime. This is consistent with findings of other researchers as mentioned in the introduction section, table 1 and in section 1.1.

Figure 8 shows the static pressure on all the faces of the cavity as a function of changing yaw angle. In figures 8b – 8e, the cavity is rotated while keeping the orientation axis fixed to show the orientation of cavity w.r.t. the incoming flow in the positive *x* direction. As can be seen in the pressure contours above, the pressure on the cavity trailing edge reflects the shifting stagnation point due to the variation in the yaw angle and the transition of the flow from an open type to a closed type. It also confirms that for a transition from $0^0$ and $90^0$ configurations, the flow begins as highly two-dimensional at $0^0$ and ends as a three-dimensional but symmetric in nature as the yaw angle approaches $90^0$.

Figure 9 traces the transition of cavity trailing edge from yaw $0^0$ to $90^0$, through the variation in pressure along the edge. In figure 9, the trailing edge at $0^0$ configuration (see figure 8a) is followed through its variation in yaw angles, i.e. the pressure on the trailing edge is plotted against $\phi$ as the edge moves from figures 8a to 8f. The rear-wall, with the trailing edge, in figure 8a becomes the side-wall in figure 8f. It can be seen from figure 9, that at $0^0$ the pressure distribution is constant along the width of the cavity, whereas at $90^0$, the pressure is lower at low $\phi$ and higher at larger $\phi$. This is because at $90^0$ the edge being plotted is now the side wall of the cavity and shows the pressure variation observed along the longitudinal direction of the flow, as confirmed by figures 7f and 8f. This phenomenon of pressure variation along the edge w.r.t. $\phi$ is also seen at intermediate yaw angles. However, at these angles the edge is still partially a trailing edge and partially a side-wall edge, as seen in figures 8b to 8e. Hence in figure 9, the pressure differential is more at the transition yaw angles. It also shows how the stagnation region on the trailing edge of the cavity moves from $\phi\, 0^0$ to $\phi\, 90^0$. The trailing edge in figure 9 at $\phi\, 90^0$ is now parallel to the incoming flow, hence the pressure variation shown in figure 9 is the variation in pressure from the leading edge to the trailing edge, as the direction vector moves along positive *w/W*.

Figure 10 shows the coefficient of drag, $C_d$, normalized by maximum $C_d$ ($C_d/C_{d\_max}$) plotted against $\phi$ for an *L/D* ratio of 16.25 and *L/W* ratio of 8.125 at $90^0$ degrees. This data is plotted over Weighardt's [1] experimental results for the same *L/D* and *L/W* ratios. The trend lines align quantitatively very well with the experimental data after a yaw of $50^0$ meanwhile the general trend of the curve qualitatively aligns well throughout the plot. The drag tends to increase as the yaw angle is increased as seen from figure 10. However, the rate of increase of drag is not constant throughout. For lower values of $\phi$, the increase in drag is much slower as compared to the mid-range of $\phi$ values, around $20^0$ to $70^0$, where the increase is more rapid. The rate of increase then again tends to plateau out as $\phi$ approaches $90^0$. This is also corroborated by Weighardt's [1] data in figure 10. The increase in drag with the increase in yaw angle for the given *L/D* and *L/W* ratios suggest that the drag increases as the flow becomes more closed or transitions towards becoming more closed in nature. This would suggest that the cavities with higher effective *L/W* ratios would have higher drag compared to those with lower effective *L/W* ratios. Figure 10 also suggest that the drag increase is high for highly yawed cavities and the three-dimensionality of yawed cavities has a significant effect on the rate of rise of drag generated within the cavity.
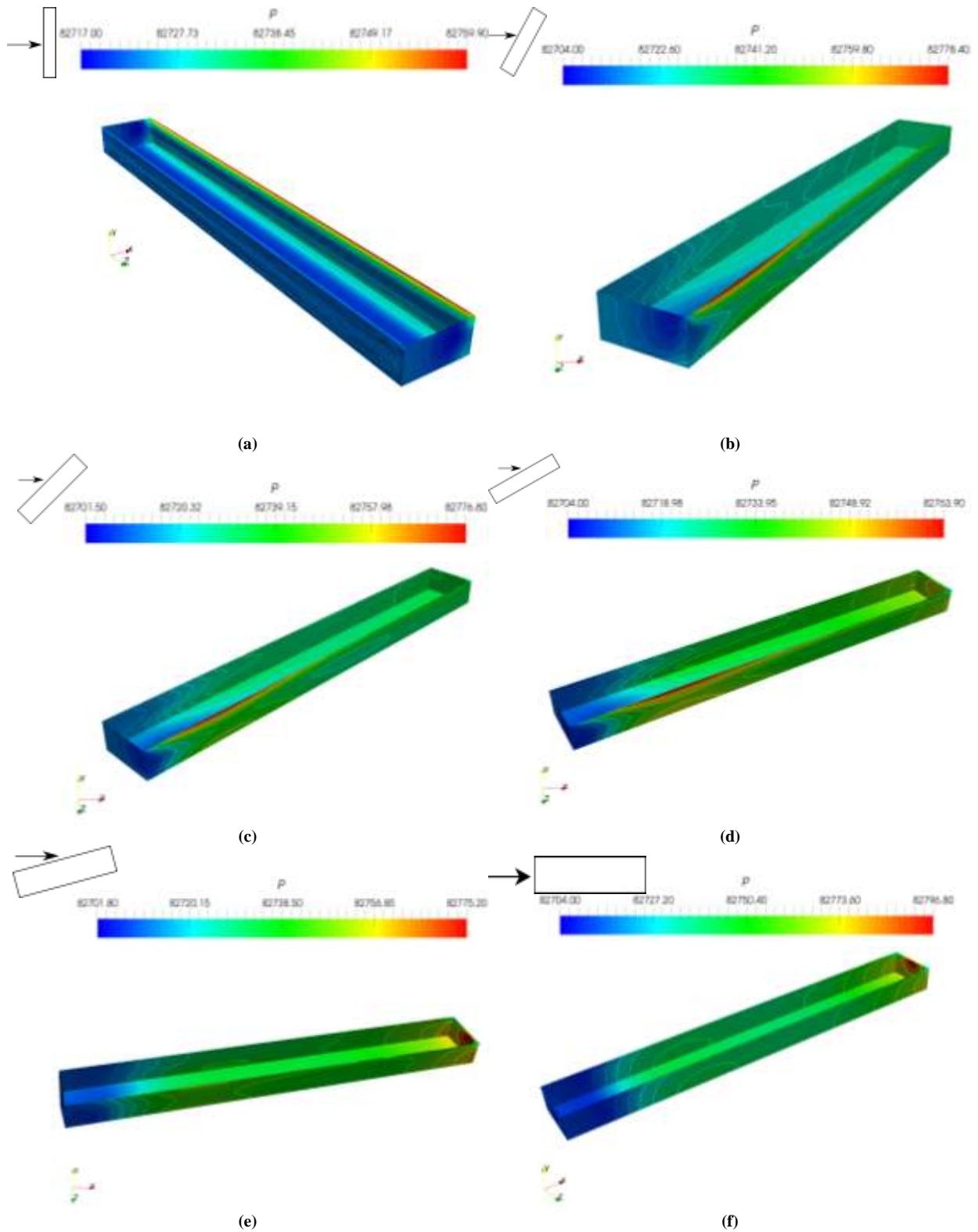
**(a)**

**(b)**

**(c)**

**(d)**

**(e)**

**(f)**

**Figure 8.** Pressure contours within the cavity at (a) $\phi\,0^0$ (b) $\phi\,30^0$ (c) $\phi\,45^0$ (d) $\phi\,60^0$ (e) $\phi\,75^0$ (f) $\phi\,90^0$
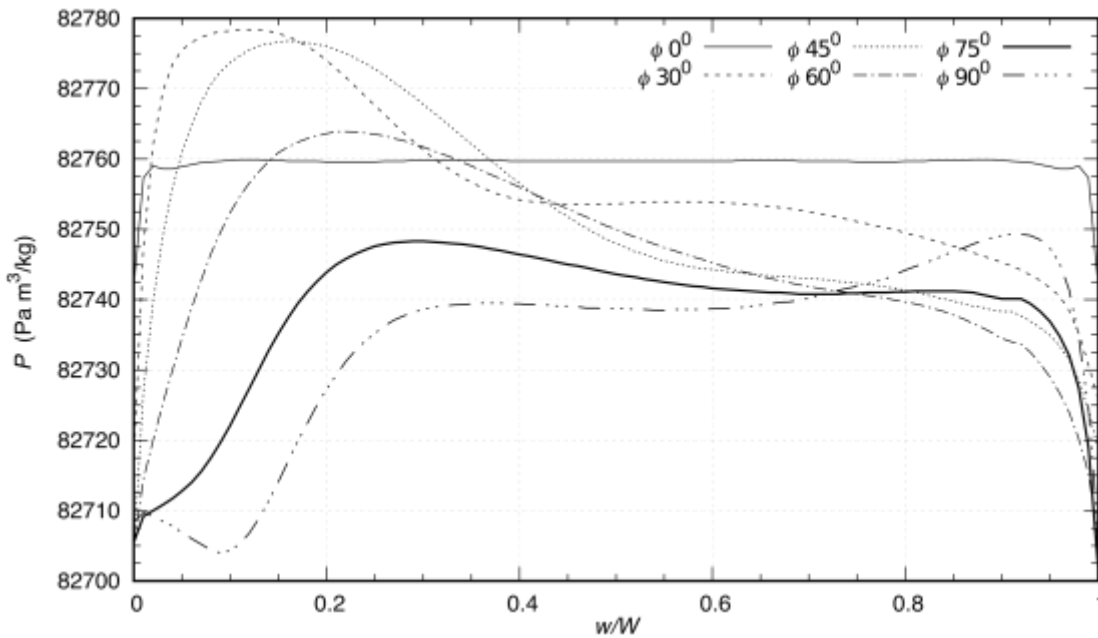
**Figure 9.** Pressure at long trailing edge w.r.t $\phi$, $w$ is width along $z$ direction, $W$ is total width of the cavity
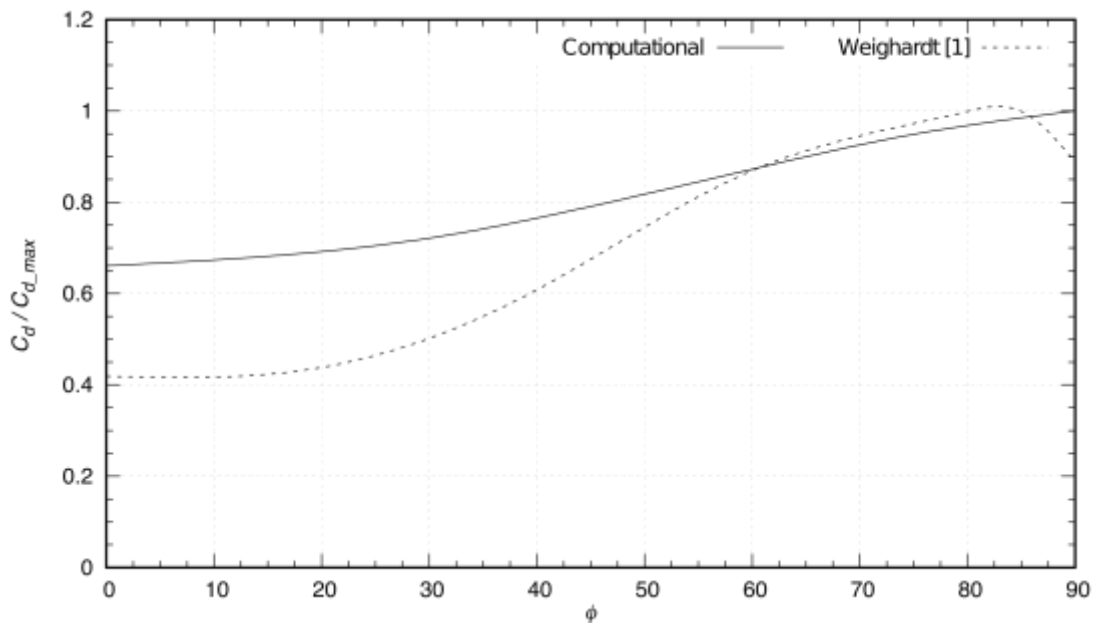


**Figure 10.** Co-efficient of drag generated within the cavity at various yaw angles

## V. CONCLUSION

A computational study on the effect of yaw angle on the drag generated by the presence of a clean sharp edged rectangular cavity imbedded in a fully developed turbulent boundary layer, of thickness $\delta = 71.46$ mm, was carried out using the open source CFD tool, OpenFOAM. Three-dimensional steady state simulations were performed on a rectangular cavity with an effective $L/D$ ratio of 16.25 and an effective $L/W$ ratio of 8.125 at a yaw angle of ninety degrees. The simulations were performed using the $k$-$\varepsilon$ turbulence model and with a free-stream velocity of 25 m/s. The pressure profile on the cavity faces were studied at yaw angles ($\phi$) of $0^0$, $30^0$, $45^0$, $60^0$, $75^0$, & $90^0$. This pressure data was also used to compute the drag generated by the presence of the cavity and the effect of yaw angle on the drag. The results were compared to the experimental results of Weighardt [1] and the data shows good agreement. From the study of pressure profiles on the cavity faces it was seen that the flow shows open type [5] characteristics at $0^0$ and goes into transition which then ends as a closed type flow at $90^0$. In addition, the flow shows highly two-dimensional behavior at $0^0$ and the three-dimensional effects

increase as the yaw angle is increased further. As the flow approaches $90^0$, the pressure data suggests a symmetry in the flow characteristic while still being three-dimensional.

The drag data shown in figure 10, shows the increase in drag generated due to the presence of the cavity as the yaw angle is increased. This increase in drag plateaus as the yaw angle approaches $90^0$, suggesting the effect of symmetry on the reduction in drag generated due to the presence of the cavity. From the simulations performed for the above study, the author also concluded that the drag characteristics of a cavity with respect to yaw angle is highly dependent on the effective *L/D* and *L/W* ratios for the cavity. Further research in this area would yield a more detailed picture of the effect of yawed cavities with different *L/D* and *L/W* ratios.

# REFERENCES

[1]     K. Weighardt, "Increase in turbulent frictional resistance caused by surface irregularities," Forschungshefte fur Schiffstechnik, vol. 2, pp. 65-81, April 1953.

[2]     I. E. Rossiter, "Wind Tunnel Experiements on the Flow Field over Rectangular cavities at Subsonic and Transonic Speeds," Aeronautical Research Council, London, R&M No. 3438, Oct. 1966.

[3]     D. Rockwell and E. Naudascher, "Self-Sustained Oscillations of Impinging Free Sheer Layer," Annual Review of Fluid Mechanics, vol. 11, pp. 67-94, 1979.

[4]     S. J. Lawson and G. N. Barakos, "Review of numerical simulations for high-speed, turbulent cavity flows," Progress in Aerospace Sciences, vol. 47, pp. 186-216, Feb. 2011.

[5]     ESDU, "Aerodynamics and aero-acoustics of rectangular planform cavities. Part I: time-averaged flow," Technical Report 02008, ESDU International; 2004.

[6]     R. L. Stalings, E. B. Plentovich, M. B. Tracy, and M. J. Hemsch, "Measurements of store forces and moments and cavity pressures for a generic store in and near a box cavity at subsonic and transonic speeds," Technical Report No. NASA-TM-4611, NASA, 1995.

[7]     X. Gloerfelt, "Cavity Noise," VKI Lecture: Aerodynamic noise from wall bounded flows, 2009 Available: http://citeseerx.ist.psu.edu/viewdoc/download?doi=10.1.1.466.1944&rep=rep1&type=pdf [last-viewed: 16 July 2017]

[8]     F. M. White, Viscous Fluid Flow, 2nd ed. McGraw-Hill, New York, 1991, pp. 409 and 413.

[9]     D. Rockwell and E. Naudascher, "Review – Self-Sustaining Oscillations of Flow Past Cavities", Journals of Fluids Engineering, vol. 100, June 1978.

[10]    P. J. Disimile, N. Toy, and E. Savory, "Pressure Oscillations in a Subsonic Cavity at Yaw," AIAA Journal, Vol. 36, No. 7, July 1998.

[11]    P. J. Disimile, X. Bai, and N. Toy, "Pressure Oscillations within a Yawed Rectangular Cavity in Subsonic Flow," International Journal of Engineering Research & Industrial Applications (IJERIA), Vol. 5, No. II, pp. 27-50, May 2012.

[12]    X. Gloerfelt, C. Bogey, and C. Bailly, "Cavity noise," Laboratoire de M´ecanique des Fluides et d'Acoustique , Ecole Centrale de Lyon & UMR CNRS 5509, 69134 Ecully, France, Available: https://www.researchgate.net/profile/Xavier_Gloerfelt/publication/226841604_Large_Eddy_Simulations_of_high_Reynolds_number_cavity_flows/links/564471b608aef646e6cae781/Large-Eddy-Simulations-of-high-Reynolds-number-cavity-flows.pdf [last-viewed: 16 July 2017]

[13]    B. E. Launder and B. I. Sharma, "Application of the Energy Dissipation Model of Turbulence to the Calculation of Flow Near a Spinning Disc," Letters in Heat and Mass Transfer, vol. 1, no. 2, pp. 131-138, 1974.

[14]    D. Wilcox, "Re-assessment of the scale-determining equation for advanced turbulence models," AIAA Journal, vol. 26, no. 11, pp. 1299-1310, 1988.

[15]    F. R. Menter, "Two-Equation Eddy-Viscosity Turbulence Models for Engineering Applications," AIAA Journal, vol. 32, no. 8, pp. 1598-1605, 1994.

[16]    The OpenFOAM Foundation, "OpenFOAM – User Guide 4.0," June 2016, Available: http://foam.sourceforge.net/docs/Guides-a4/OpenFOAMUserGuide-A4.pdf [last-viewed: 16 July 2017]